Organic Electronics 118 (2023) 106796

Contents lists available at ScienceDirect

Organic Electronics

journal homepage: www.elsevier.com/locate/orgel

Three- and two-dimensional mixed metal halide perovskites for high-performance photovoltaics

Lening Shen [a,1], Haodong Wu [a,1], Tao Zhu [a], Xinwen Zhang [b], Hussain Sawwan [a], He Wang [b,**], Xiong Gong [a,*]

[a] School of Polymer Science and Polymer Engineering, College of Engineering and Polymer Science, The University of Akron, Akron, OH, 44325, USA
[b] Department of Physics, University of Miami, Coral Gables, Florida, 33146, USA

ARTICLE INFO

Keywords:
Perovskite photovoltaics
2D:3D mixed perovskite composites
Efficiency
Detectivity
Stability

ABSTRACT

Three-dimensional (3D) metal halide perovskites (MHPs) incorporated with two-dimensional (2D) MHPs have been demonstrated to be a facile way to approach the high performance of perovskite photovoltaics (PPVs). In this study, we report high-performance PPVs, in terms of efficiency, detectivity, stability, and photocurrent hysteresis, based on the 3D mixed with 2D MHPs composites (termed as the 2D:3D mixed MHPs composites), where 4-fluoro-phenethylammonium, which possesses larger dipole moment compared to phenethylammonium, is used to create 2D MHPs. Systematically studies indicate that the 2D:3D mixed MHPs composites possess larger crystals, higher crystallinity, and enhanced charge transport compared to 3D MHPs thin film. As a result, the PPVs based on the 2D:3D mixed MHPs composites exhibit over 21.16 ± 0.53% power conversion efficiency with suppressed photocurrent hysteresis, over 10^{16} cm $Hz^{1/2}W^{-1}$ detectivity, and dramatically boosted stability. Our results indicate that we provide a facile way to approach high-performance PPVs.

1. Introduction

In the past years, metal halide perovskites (MHPs) have drawn great attention in both academic and industrial sectors due to their super optoelectronic properties [1,2]. Over 25% power conversion efficiency (PCEs) and 10^{15} Jones (1 Jones = 1 cm $Hz^{1/2}W^{-1}$) detectivity have been reported from perovskite photovoltaics (PPVs) based on the three-dimensional (3D) MHPs [3,4]. However, studies indicated that 3D MHPs are sensitive to moisture, oxygen, and light, restricting their practical applications [5–7]. Interfacial engineering [8–10], structural and compositional engineering [11–14], and encapsulating technology [15–17] have been attempted to boost the stability of PPVs. For example, Fu et al. applied polyethylene glycol additive into MHPs precursor solution to prepare high-quality of MHPs thin films for approaching the high-performance PSCs [9]. On the other hand, the utilization of large-sized hydrophobic organic ammonium to substitute small-sized hydrophilic organic ammonium within 3D MHPs, creating two-dimensional (2D) MHPs, was demonstrated to be a facile way to approve stable PPVs [18–26]. Mohite et al. reported a PCE of 12.51% from the perovskite solar cells (PSCs) based on the 2D $(BA)_2(MA)_2Pb_3I_{10}$ (where BA is n-butylammonium and MA is methylammonium) thin films [22]. Yao et al. demonstrated a PCE of 14.68% from the PSCs based on the 2D $(TEA)_2(MA)_2Pb_3I_{10}$ thin film (where TEA is 2-thiophene ethylamine) and further found that PSCs could maintain 93% of their initial PCEs after 500 h in an ambient condition [23]. Wang et al. reported over 20.3% PCE with improved stability from the PSCs based on the PA-based 2D MHPs over the 3D MHPs thin film (where PA is n-propylammonium) [25]. Recently, we reported over 23% PCE from the PSCs based on the $PEA_2PbBr_{0.3}I_{3.7}/MAPbBr_{0.3}I_{2.7}$ thin film (where PEA is phenethylammonium) [26]. On the other hand, the perovskite photodetectors (PPDs) based on the 2D/3D bilayer MHPs thin films have also received great attention [27–29]. Luo et al. presented a detectivity of over 10^{12} Jones from the PPDs based on the $(4\text{-AMP})(MA)_2Pb_3Br_{10}/MAPbBr_3$ bilayer MHPs thin films (where 4-AMP is 4-(aminomethyl) piperidinium) [29]. We also reported a photoresponsivity of 1.38 AW^{-1}, a detectivity of 6.52×10^{14} Jones, and a linear dynamic range of over 167 dB at room temperature from the PPDs based on the $PEA_2PbI_4/MAPbI_3$ MHPs bilayer thin film, where the MHPs bilayer thin film was

* Corresponding author.
** Corresponding author.
E-mail addresses: hewang@miami.edu (H. Wang), xgong@uakron.edu (X. Gong).
[1] These authors contributed to this work equally.

https://doi.org/10.1016/j.orgel.2023.106796
Received 11 December 2022; Received in revised form 15 March 2023; Accepted 17 March 2023
Available online 23 March 2023

post-treated with 1-butanol vapor [27].

In this study, we report high-performance PPVs, in terms of efficiency, detectivity, stability, and photocurrent hysteresis, based on the 3D mixed with 2D MHPs composites, where the 2D MHPs are based on 4-fluoro-phenethylammonium (4F-PEA) as the organic spacer. 4F-PEA is selected as organic spacer to create 2D (4F-PEA)PbI_4 since it has two functionalities. One is that the F atoms within 4F-PEA could form hydrogen bonds with H atoms, resulting in optimizing the intermolecular packing [30]. Another is that the 4F-PEA cations have a large dipole moment compared to PEA [31], which could restrict the dielectric confinement effect and decrease the exciton binding energy. Both of them could boost charge carrier dissociation, resulting in enhanced device performance of PPVs [21]. Our systematic studies indicate that the $(4F\text{-}PEA)_2PbI_4$:$MAPbI_3$ thin film indeed possesses larger crystals, higher crystallinity, and enhanced charge transport compared to 3D $MAPbI_3$ thin film. As a result, the PPVs based on the $(4F\text{-}PEA)_2PbI_4$:$MAPbI_3$ thin film exhibit a PCE of 21.16 ± 0.53% % with suppressed photocurrent hysteresis, over 10^{16} Jones detectivity, and dramatically boosted stability.

2. Experimental section

2.1. Materials

Poly[bis(4-phenyl)(2,4,6-trimethylphenyl)amine] (PTAA), Gamma-butyrolactone (GBL, 99%), 4-fluorophenethylamine (4F-PEA, 99%), anhydrous toluene (99.8%), methylamine (33 wt % in absolute ethanol), bathocuproine (BCP, 99.99%), anhydrous acetonitrile (ACN, 99.8%) were purchased from Sigma-Aldrich. C_{60} was bought from 1-Material, Inc. Lead iodide (PbI_2, 99.9985% metals basis) was purchased from Alfa Aesar. Methylammonium iodide (CH_3NH_3I (MAI)) was purchased from Greatcell Solar Materials. All materials were used as acquired without further processing.

2.2. Preparation of the $MAPbI_3$ single crystals

The inverse temperature crystallization method was used to prepare the $MAPbI_3$ single crystals [31]. In brief, 1 mmol MAI and 1 mmol PbI_2 were dissolved into 1 mL GBL solvent to get the precursor solution. Then the precursor solution was kept heating and stirring until a yellow color clear solution was obtained. Afterward, the clear solution was heated until the temperature reaches 110 °C. At this condition, the $MAPbI_3$ single crystals would grow naturally. After 12 h, shape-regular black--color single crystals were formed and then washed with isopropanol solvent (IPA), followed by drying in the oven for 10 min (mins).

2.3. Preparation of perovskite precursor solution

The preparation of the $MAPbI_3$ ACN solution followed the previous report [32]. Briefly, the $MAPbI_3$ single crystals were put into a small vial with a cap open, and the small vial was placed into a large vial in which there was a certain amount of methylamine ethanol solution. In this way, the $MAPbI_3$ single crystals could be exfoliated by the methylamine vapor and a viscous yellowish solution was obtained. Then the ACN solvent was added to the viscous solution to acquire the 1 mol/L $MAPbI_3$ ACN precursor solution. For the 4F-PEA-based 2D:3D mixed perovskite solution, the specific amount of 4F-PEA (consistent with the molar ratios of 4F-PEA to $MAPbI_3$) was directly added to the $MAPbI_3$ ACN precursor solution.

2.4. Preparation and characterizations of perovskite thin films

Both 3D $MAPbI_3$ thin film and the 2D:3D mixed perovskite thin film were spin-coated onto the glass substrate at a speed of 6000 rpm for 30 s (s) from their corresponding precursor solutions, followed by the thermal annealing at 100 °C for 10 min. X-ray diffraction (XRD) measurements were conducted by applying a Bruker AXS Dimension D8 X-ray system. The photoluminescence (PL) spectra of different perovskite thin films were measured on a HORIBA Fluorolog-3 fluorescence spectrophotometer. The ultraviolet–visible (UV–vis) absorption spectra of different perovskite thin films were measured on the HP 8453 spectrophotometer. A field-emission scanning electron microscope (SEM) (JEOL-7401) was conducted to acquire the top-view SEM images. The grazing-incidence wide-angle x-ray scattering (*GIWAXS*) profile was measured by using the specific beamline (Sector 8-ID-E) in the Advanced Photon Source (APS), Argonne National Laboratory [33]. Femtosecond laser transient absorption spectra (ultrafast systems) were obtained with a pump beam at 400 nm and a probe beam of white light, with the details, reported elsewhere [34].

2.5. Fabrication of perovskite photovoltaics

Firstly, the pre-cleaned indium tin oxides (ITO) coated glass substrates were processed in the UV/Ozone in an ambient environment for 20 min. After this treatment, approximately ~8 nm PTAA layer was spin-coated onto the top of the ITO/glass substrate from 2 mg/mL PTAA toluene solution at 6000 rpm for 40 s (s) and then thermal annealed at 100 °C on a hotplate for 10 min in a glovebox with a nitrogen atmosphere and then cooled down to room temperature (*RT*). The perovskite layer was spin-coated at a speed of 6000 rpm for 30 s from their corresponding precursor solutions, followed by thermal annealing at 100 °C on a hotplate for 10 min. Lastly, a ~15 nm thick C_{60}, an ~8 nm BCP, and a ~120 nm Ag were subsequently thermally deposited in a specific chamber at the air pressure of 1×10^{-5} mbar. The complete device active area was measured to be 0.043 cm^2.

2.6. Characterization of perovskite photovoltaics

The current density versus voltage (J-V) characteristics of PSCs was recorded on a Keithley model 2400 source measure unit in dark and under light with a solar simulator (AM1.5 G) as the light source. The light intensity of the source was calibrated to be 100 mW/cm^2 by using a mono silicon reference cell, which was purchased from the National Renewable Energy Laboratory (NREL). The J-V characteristics of PPDs were conducted on the same setup under white light with a light intensity of 100 mW/cm^2, monochromatic light at a wavelength $\lambda = 500$ nm with a light intensity of 0.28 $mW/cm^{2,}$ and in dark. The external quantum efficiency (EQE) spectra were measured on the solar cell quantum efficiency measurement system (QEX10) with a stable xenon lamp as the optical source at 0 or - 0.1 V bias. The impedance measurements of cells were operated on an HP 4194A impedance/gain-phase analyzer in the dark. During the measurement, the applied voltage for PSCs was on the verge of the relevant V_{OC} of each device. Both the capacitor versus voltage (C–V) and the capacitor versus frequency (C–F) characteristics were performed on the same setup by applying Keithley model 82-WIN Simultaneous CV (CF) System. The photocurrent hysteresis measurement was conducted by tuning the scan directions including reverse scan and forward scan. The photocurrent response time measurement during the photocurrent rising process of PSCs was performed on a homemade setup by applying an optical chopper-controlled laser pulse ($\lambda = 532$ nm) at a frequency of 2 kHz.

3. Results and discussion

Scheme 1 displays the top-view SEM images of the 3D $MAPbI_3$ and $(4F\text{-}PEA)_2PbI_4$:$MAPbI_3$ thin films. Many small crystals with a crystal size of ~100 nm are observed from the 3D $MAPbI_3$ thin film, whereas, different film morphology and crystal size are observed from the 2D $(4F\text{-}PEA)_{1+x}PbI_{3+x}$ (where x is the molar ratio of 4F-PEA, x = 0.6, 1.0, and 1.5) mixed with the 3D $MAPbI_3$ thin film (termed as [$(4F\text{-}PEA)_{1+x}Pb_nI_{3+x}$:$MAPbI_3$] (Scheme S1). In particular, as x = 1, a rough surface and large crystals (~500 nm) are observed from the (4F-

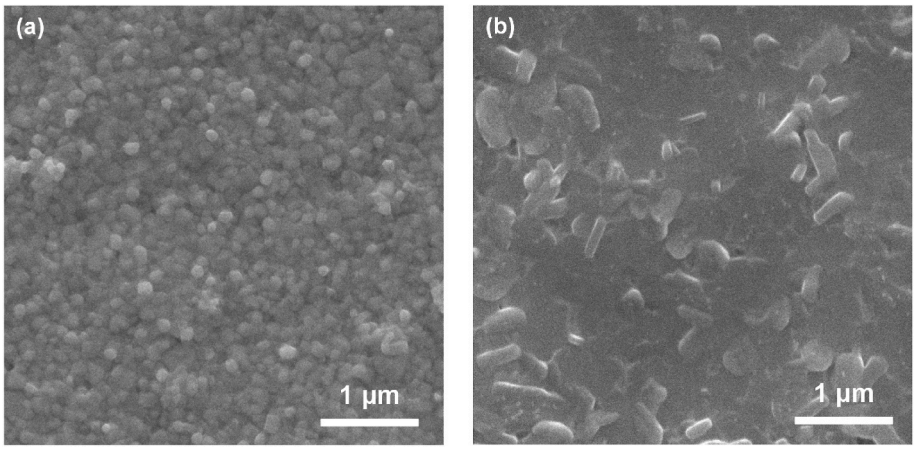

Scheme 1. The top-view SEM images of (a) $MAPbI_3$ and (b) $(4F\text{-}PEA)_2PbI_4$:$MAPbI_3$ thin films.

PEA)$_2$PbI$_4$:MAPbI$_3$ thin film. These results indicate that 4F-PEA organic spacer could tune the grain size of the resultant $(4F\text{-}PEA)_2PbI_4$:$MAPbI_3$ thin film.

It is found that the shapes of absorption spectra of the 3D $MAPbI_3$ thin film and the $(4F\text{-}PEA)_{1+x}PbI_{3+x}$:$MAPbI_3$ thin films coated on the glass substrates are nearly identical (Fig. 1a and Fig. S1a). The steady-state photoluminescence (PL) spectra of the 3D $MAPbI_3$ thin film and the $(4F\text{-}PEA)_2PbI_4$:$MAPbI_3$ thin film coated on the glass substrates are shown in Fig. 1b. Under the excitation from the front side of MHPs thin film, an obvious emission peak located at the wavelength (λ) of 610 nm is observed from the $(4F\text{-}PEA)_2PbI_4$:$MAPbI_3$ thin film, whereas no emission peaked at $\lambda = 610$ nm is presented in the 3D $MAPbI_3$ thin film. The emission peak at λ of 610 is attributed to the $(4F\text{-}PEA)_2PbI_4$ [31,35]. An emission peak located at λ of 610 nm is also observed from the $(4F\text{-}PEA)_2PbI_4$:$MAPbI_3$ thin film as it is excited from the back side (glass side), which illustrates that the layered 2D $(4F\text{-}PEA)_2PbI_4$ is formed within the 3D $MAPbI_3$ thin film [21,31]. Moreover, an emission peak located at 735 nm observed from the $(4F\text{-}PEA)_2PbI_4$:$MAPbI_3$ thin film indicates the existence of $(4F\text{-}PEA)_x(MAPbI_3)_{1\text{-}x}$ due to multiple *n* values coexisted in the MHPs [31,35]. In addition, the PL intensities at λ of 610 nm from the $(4F\text{-}PEA)_{1+x}PbI_{3+x}$:$MAPbI_3$ (where x = 0.6, 1.0, and 1.5) thin films are nearly the same as they are excited from the front side, but are increased and then decreased for the $(4F\text{-}PEA)_{1+x}PbI_{3+x}$:$MAPbI_3$ thin films along with increased concentrations of 4F-PEA as they are excited from the back side (Figs. S1b and c). However, there is an emission peak located at 840 nm observed from $(4F\text{-}PEA)_{1+x}PbI_{3+x}$:$MAPbI_3$ thin films. This peak is probably ascribed to the interface between 2D $(4F\text{-}PEA)_{1+x}PbI_{3+x}$ and 3D $MAPbI_3$ [21,35]. Nevertheless,

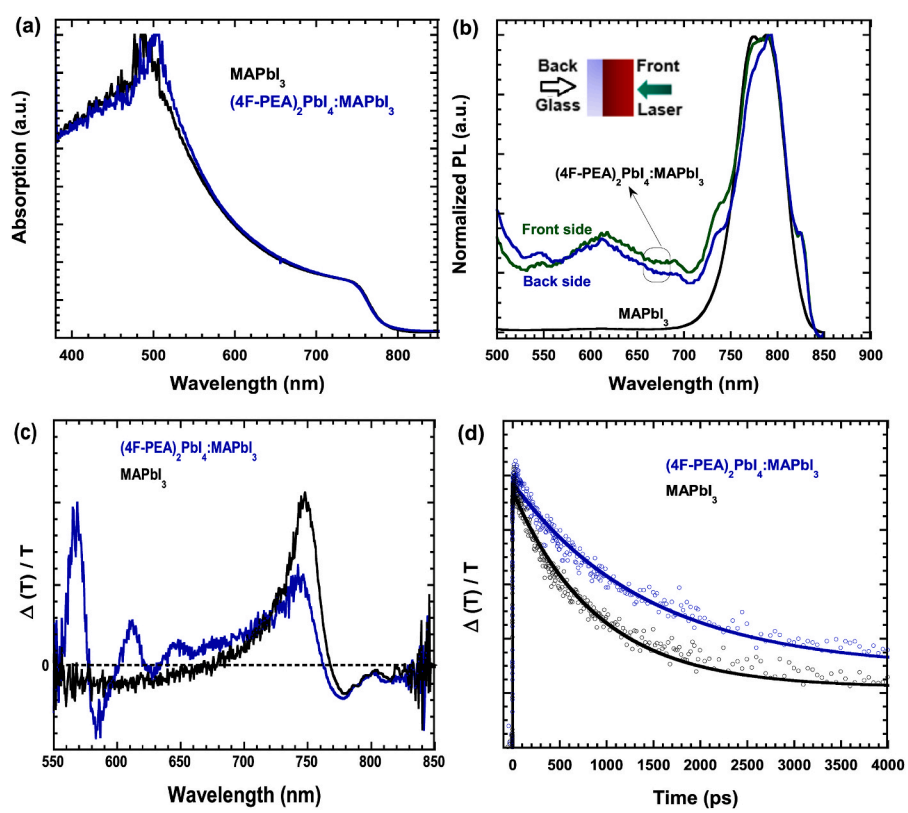

Fig. 1. (a) Absorption, (b) photoluminescence (PL) spectra, (c) the corrected femtosecond transient absorption (TA) spectroscopies, and (d) the TA kinetics of $MAPbI_3$ and $(4F\text{-}PEA)_2PbI_4$:$MAPbI_3$ thin films.

these results further indicate that the 2D $(4F\text{-}PEA)_{1+x}PbI_{3+x}$ (where x = 0.6, 1.0, and 1.5) crystals are formed within the 3D $MAPbI_3$ thin film, but with different film morphologies (Scheme 1 and Scheme S1).

The corrected femtosecond transient absorption (TA) spectra of the 3D $MAPbI_3$ and $(4F\text{-}PEA)_2PbI_4$:$MAPbI_3$ thin films are shown in Fig. 1c. Both thin films show similar ground-state bleaching (GSB) peaks, but with different locations. The GSB peak for the 3D $MAPbI_3$ thin film is located at λ of 748.4 nm, whereas the GSB peak for the $(4F\text{-}PEA)_2PbI_4$:$MAPbI_3$ thin film is located at λ of 746.6 nm. Moreover, compared to 3D $MAPbI_3$ thin film, three peaks located at λ of 568.7 nm, 612.1 nm, and 648 nm are observed from the $(4F\text{-}PEA)_2PbI_4$:$MAPbI_3$ thin film, which further indicates that 2D $(4F\text{-}PEA)_2PbI_4$ is formed within $(4F\text{-}PEA)_2PbI_4$:$MAPbI_3$ thin film.

Fig. 1d presents the TA kinetics of the 3D $MAPbI_3$ and $(4F\text{-}PEA)_2PbI_4$:$MAPbI_3$ thin films. The kinetics fitting of the 3D $MAPbI_3$ thin film at λ of 748 nm exhibits a long lifetime of 0.9 ns (ns); whereas a slower decay kinetic process with a long lifetime of 1.4 ns is observed from the $(4F\text{-}PEA)_2PbI_4$:$MAPbI_3$ thin film. Such a long lifetime indicates that the $(4F\text{-}PEA)_2PbI_4$:$MAPbI_3$ thin film possesses large crystal sizes and suppressed defects [36], which are consistent with the SEM observation. Moreover, such a long lifetime also indicates that the nonradioactive charge recombination is suppressed in the $(4F\text{-}PEA)_2PbI_4$:$MAPbI_3$ thin film compared to the 3D $MAPbI_3$ thin film [37]. Thus, the PPVs based on the $(4F\text{-}PEA)_2PbI_4$:$MAPbI_3$ thin film are expected to exhibit enhanced device performance as compared to that based on the 3D $MAPbI_3$ thin film.

The XRD patterns of the 3D $MAPbI_3$ thin film and the $(4F\text{-}PEA)_{1+x}PbI_{3+x}$:$MAPbI_3$ (x = 0.6, 1.0, 1.5) thin films are shown in Fig. 2 (and Fig. S2). Major peaks that appeared in these thin films are identical. Two peaks located at ~14° and ~28° correspond to the (110) and the (220) planes, respectively, which are consistent with previous reports and indicate that both the 3D $MAPbI_3$ thin film and the $(4F\text{-}PEA)_{1+x}PbI_{3+x}$:$MAPbI_3$ (x = 0.6, 1.0, 1.5) thin films possess the tetragonal crystal structure [32,38]. However, compared to the 3D $MAPbI_3$ thin film, a small peak located at ~5.5° corresponding to the (002) crystal plane, is observed from the $(4F\text{-}PEA)_{1+x}PbI_{3+x}$:$MAPbI_3$ (x = 0.6, 1.0, 1.5) thin films. In addition, a tiny peak next to the (220) plane is observed from the $(4F\text{-}PEA)_{1+x}PbI_{3+x}$:$MAPbI_3$ (x = 0.6, 1.0, 1.5) thin films. All these indicate that $(4F\text{-}PEA)_{1+x}PbI_{3+x}$ are formed the 2D phase [26].

Moreover, the full width at half maximum (FWHM) of the peak at the (110) plane for the $(4F\text{-}PEA)_2PbI_4$:$MAPbI_3$ thin film is 0.146°, which is smaller than that (0.168°) for the 3D $MAPbI_3$ thin film. A smaller FWHM value indicates the crystal size of the $(4F\text{-}PEA)_2PbI_4$:$MAPbI_3$ thin film is larger than that of the 3D $MAPbI_3$ thin film. These observations are consistent with the SEM results.

The GIWAXS measurement is carried out to differential the crystal orientation and crystallinity of the 3D $MAPbI_3$ and $(4F\text{-}PEA)_2PbI_4$:$MAPbI_3$ thin films, and the results are shown in Fig. 2b and c. The 3D $MAPbI_3$ thin film shows strongly scattered rings all reflections along the scattering vector, which represents the randomly oriented features of the 3D $MAPbI_3$. However, a mixture of scattered secondary spots and rings are observed in the $(4F\text{-}PEA)_2PbI_4$:$MAPbI_3$ thin film, which demonstrates that the $(4F\text{-}PEA)_2PbI_4$ thin film has a stronger crystal orientation. The line cut of the GIWAXS patterns of these two thin films is shown in Fig. 2d. The intensity at $q_z = 1$ (corresponding to the (110) plane) of the $(4F\text{-}PEA)_2PbI_4$:$MAPbI_3$ thin film is higher than that of the 3D $MAPbI_3$ thin film, and the FWHM values of the peak located at 1 A^{-1} of the $(4F\text{-}PEA)_2PbI_4$:$MAPbI_3$ thin film is smaller (~0.04 A^{-1}) than that (~0.06 A^{-1}) of the 3D $MAPbI_3$ thin film. These results further demonstrate that the $(4F\text{-}PEA)_2PbI_4$:$MAPbI_3$ thin film possesses better crystallinity, which is favorable for the PPVs based on the $(4F\text{-}PEA)_2PbI_4$:$MAPbI_3$ thin film exhibiting a boosted short-circuit current (J_{SC}).

Fig. 3a shows the J-V characteristics of the PSCs with a device structure of ITO/PTAA/perovskites/C_{60}/BCP/Ag (Scheme S2),

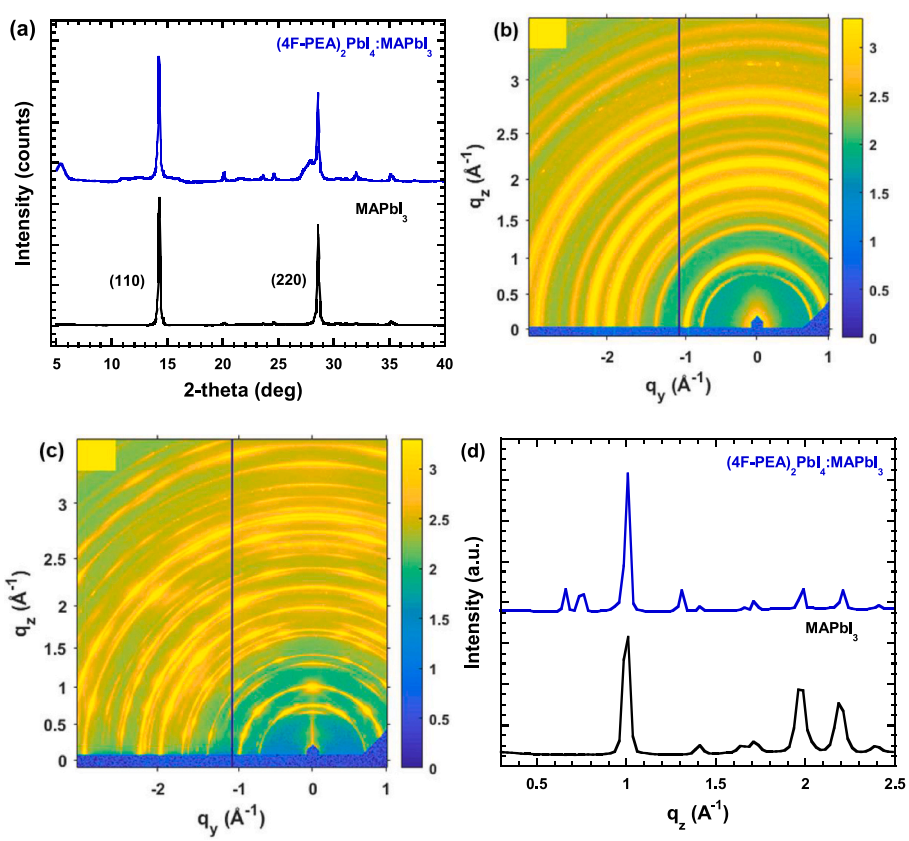

Fig. 2. (a) The XRD patterns of $MAPbI_3$ and $(4F\text{-}PEA)_2PbI_4$:$MAPbI_3$ thin films, the GIWAXS patterns of (b) $MAPbI_3$ and (c) $(4F\text{-}PEA)_2PbI_4$:$MAPbI_3$ thin films, (d) the line cut of the GIWAXS patterns of $MAPbI_3$ and $(4F\text{-}PEA)_2PbI_4$:$MAPbI_3$ thin films.

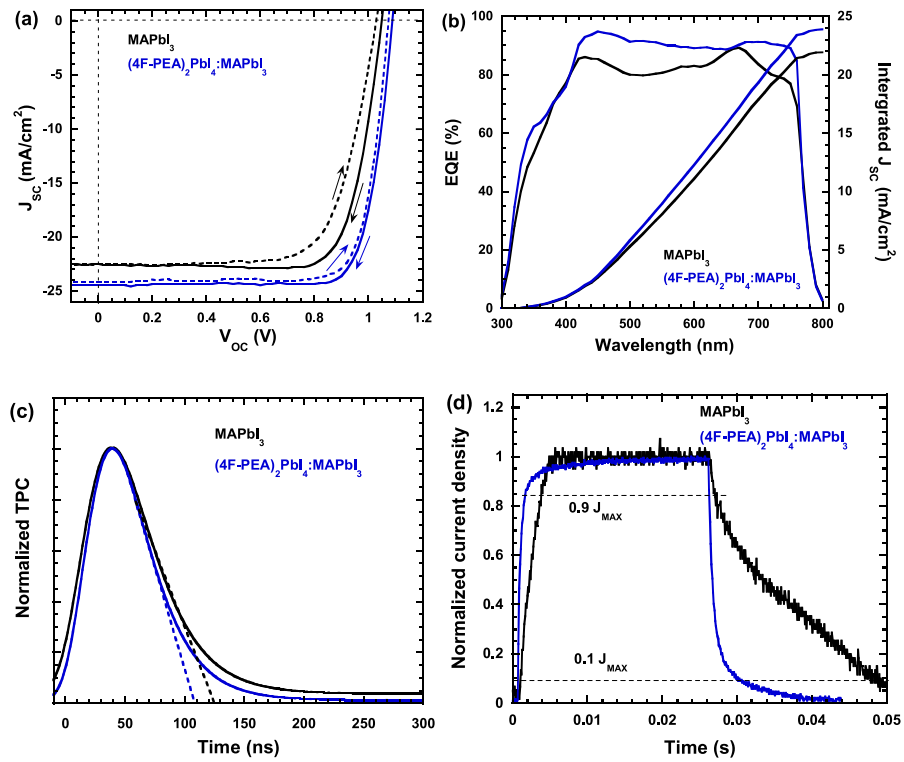

Fig. 3. (a) The J-V characteristics and (b) the external quantum efficiency (EQE) spectra, (c) the transient photocurrent (TPC) and (d) the photocurrent rising process of the PSCs, where the PSCs are fabricated by either $MAPbI_3$ thin film or $(4F\text{-}PEA)_2PbI_4$:$MAPbI_3$ thin film.

measured from both forward and reverse directions, where ITO acts as the anode, PTAA is used as the hole extraction layer (HEL), perovskites are either the 3D $MAPbI_3$ thin film or the $(4F\text{-}PEA)_2PbI_4$:$MAPbI_3$ thin film, C_{60} acts as the electron extraction layer (EEL), BCP acts as the hole-block layer, Ag acts as the cathode, respectively. The PSCs based on the 3D $MAPbI_3$ exhibit an open-circuit voltage (V_{OC}) of 1.04 ± 0.01 V, a J_{SC} of 22.51 ± 0.08 mA cm^{-2} and a fill factor (FF) of 78 ± 06%, with a corresponding PCE of 18.26 ± 0.45%. These device performance parameters are consistent with those reported values [27,39]. The PSCs based on the $(4F\text{-}PEA)_{1+x}PbI_{3+x}$:$MAPbI_3$ (x = 0.6, 1.0, and 1.5) thin films exhibit different device performances (Fig. S3 and Table S1). The best device performance is observed from the PSCs based on the $(4F\text{-}PEA)_2PbI_4$:$MAPbI_3$ thin film, which exhibits a V_{OC} of 1.08 ± 0.01 V, a J_{SC} of 24.48 ± 0.34 mA cm^{-2}, and a FF of 80 ± 0.12%, with a corresponding PCE of 21.16 ± 0.53%, resulting in a more than 15% enhancement in PCE compared to the PSCs based on the 3D $MAPbI_3$ thin film.

The photocurrent hysteresis index (HI) is used to evaluate the photocurrent hysteresis of PSCs. The HI is described as $HI = [J_{RS} * (0.8*V_{OC}) - J_{FS} * (0.8 * V_{OC})]/[J_{RS} * (0.8 * V_{OC}]$, where J_{RS}*(0.8*V_{OC}) and J_{FS}*(0.8*V_{OC}) represent the photocurrent density at 80% of V_{OC} for the reverse and forward scans, respectively [40]. The HI value for the PSCs based on the 3D $MAPbI_3$ thin film is 10.6%, which is larger than that (3.1%) from the PSCs based on the $(4F\text{-}PEA)_2PbI_4$:$MAPbI_3$ thin film. A small HI demonstrates that the PSCs based on the $(4F\text{-}PEA)_2PbI_4$:$MAPbI_3$ thin film possess suppressed photocurrent hysteresis.

Fig. 3b presents the EQE spectra of PSCs. At $\lambda < 450$ nm, the reduction in EQE values for both PSCs is due to the front surface charge recombination [41]. Compared to the PSCs based on the 3D $MAPbI_3$ thin film, the enhanced EQE values ranging from λ of 450–750 nm observed from the PSCs based on the $(4F\text{-}PEA)_2PbI_4$:$MAPbI_3$ thin film are ascribed to large crystal size and superior crystallinity of the $(4F\text{-}PEA)_2PbI_4$:$MAPbI_3$ thin film compared to the 3D $MAPbI_3$ thin film. Moreover, the integrated photocurrent densities of the PSCs based on either the 3D $MAPbI_3$ thin film or the $(4F\text{-}PEA)_2PbI_4$:$MAPbI_3$ thin film are 21.91 and 23.86 mA/cm^2, which are in good agreement with J_{SC} values obtained from the J-V characteristics (Fig. 3a).

The transient photocurrent (TPC) measurement is conducted to explore the charge generation and transport kinetics in PSCs [42,43]. Fig. 3c presents the normalized TPC curves of PSCs. Both PSCs possess a similar TPC curve. In the beginning, the linear TPC curves are observed due to the short time of charge carrier extraction [44,45]. After ~ 40 ns (ns), a significant difference happened in two different PSCs, which is ascribed to the trap and de-trap processes of charge carriers within the 3D $MAPbI_3$ and $(4F\text{-}PEA)_2PbI_4$:$MAPbI_3$ thin films [43]. By extrapolating the linear region to zero, the lifetime of charge extraction is estimated [46]. The PSCs based on the 3D $MAPbI_3$ thin film have a lifetime of ~130 ns, while the PSCs based on the $(4F\text{-}PEA)_2PbI_4$:$MAPbI_3$ thin film have a lifetime of ~105 ns. Thus, the sweep-out process of charge carrier within the PSCs based on the $(4F\text{-}PEA)_2PbI_4$:$MAPbI_3$ thin film is faster than that of the PSCs based on the 3D $MAPbI_3$ thin film [46], resulting in enhanced J_{SC} for the PSCs based on the $(4F\text{-}PEA)_2PbI_4$:$MAPbI_3$ thin film. Moreover, in comparison to the PSCs based on the 3D $MAPbI_3$ thin films, the PSCs based on the $(4F\text{-}PEA)_2PbI_4$:$MAPbI_3$ thin film possess boosted photocurrent density (Fig. S4), which indicates the charge carrier recombination within the PSCs based on the $(4F\text{-}PEA)_2PbI_4$:$MAPbI_3$ thin film is suppressed. As a result, the PSCs based on the $(4F\text{-}PEA)_2PbI_4$:$MAPbI_3$ thin film exhibit enlarged J_{SC} and boosted PCE.

Fig. 3d are the photo-response time of PSCs during the photocurrent rising process. At the times for the photocurrent reaches 10% PCE (rising) and 90% (falling) PCE [47], the PSCs based on the 3D $MAPbI_3$ thin film show a rising time of 3.1 ms (ms) and a falling time of 20.2 ms under green light illumination (λ of 532 nm), indicating there is a balanced process between the ion/vacancy migration and trap-filling phenomenon. Under the same conditions, the PSCs based on the $(4F\text{-}PEA)_2PbI_4$:$MAPbI_3$ thin film have a rising time of 1.2 ms and a falling time of 3.5 ms. Such small rising and falling times indicate that the ion/vacancy migration and trap-filling process are probably suppressed to certain

degrees. Thus, the PSCs based on the $(4F\text{-}PEA)_2PbI_4$:$MAPbI_3$ thin film exhibit enhanced J_{SC}.

Fig. 4a displays the C–V curves of PSCs. According to the $C^2 = q\varepsilon_0\varepsilon_M N_A/2(V_0 - V)$ (where C is capacitance, q is the value of elementary charge (1.6×10^{-19} C), ε_0 is vacuum permittivity (8.85×10^{-12} F/m), ε_M is the permittivity of the perovskite thin film, which is calculated based on the C–F characteristics of PSCs (Fig. S5), N_A is the trap density, V_0 is the built-in potential, V is the applied voltage), the trap density (N_A) of PSCs can be estimated from the slope of the C–V curve [48–50]. The N_A of the PSCs based on the 3D $MAPbI_3$ thin film is estimated to be 1.68×10^{11}, whereas, the N_A of the PSCs based on the $(4F\text{-}PEA)_2PbI_4$:$MAPbI_3$ thin film is estimated to be 1.413×10^{11}. Thus, compared to the 3D $MAPbI_3$ thin film, the $(4F\text{-}PEA)_2PbI_4$:$MAPbI_3$ thin film possess suppressed defects, which is beneficial for suppressing charge carrier recombination, resulting in PSCs with enhanced J_{SC} and FF. On the other hand, the built-in potential of the PSCs based on the $(4F\text{-}PEA)_2PbI_4$:$MAPbI_3$ thin film is 1.13 V, which is slightly larger than that (1.08 V) for the PSCs based on the 3D $MAPbI_3$ thin film. A large built-in potential corresponds to the PSCs with a large V_{OC} [51]. Thus the PSCs based on the $(4F\text{-}PEA)_2PbI_4$:$MAPbI_3$ thin film exhibit a larger V_{OC} compared to that based on the 3D $MAPbI_3$ thin film.

To further explore the underlying physics of boosted device performance for the PSCs based on the $(4F\text{-}PEA)_2PbI_4$:$MAPbI_3$ thin film, charge transfer resistance (R_{CT}) of PSCs is investigated and the results are shown in Fig. 4b. The R_{CT} observed from the PSCs based on the $(4F\text{-}PEA)_2PbI_4$:$MAPbI_3$ thin film is 683 Ω, which is smaller than that (803 Ω) from the PSCs based on the 3D $MAPbI_3$ thin film. Since R_{CT} is related to the interfaces between the H(E)EL and the electrodes and between the H(E)EL and the perovskite active layer [52], a smaller R_{CT} indicates the charge carrier transfer process is efficient within PSCs. A smaller R_{CT} from the PSCs based on the $(4F\text{-}PEA)_2PbI_4$:$MAPbI_3$ thin film is ascribed to the high-quality thin film and suppressed charge carrier recombination. Thus, the PSCs based on the $(4F\text{-}PEA)_2PbI_4$:$MAPbI_3$ thin film possess an enhanced J_{SC} and FF compared to the PSCs based on the 3D $MAPbI_3$ thin films.

The light intensity-dependent J_{SC} and V_{OC} are shown in Fig. 4c. Both PSCs follow the power law of $J_{SC} \propto I^{\alpha}$. where I is the light intensity and α is an index associated with bimolecular recombination [53,54]. A α of 1 indicates the bimolecular recombination is completely suppressed [53,54]. A α of 0.82 observed from the PSCs based on the 3D $MAPbI_3$ thin film indicates the bimolecular recombination is suppressed, which is probably originated from relatively large crystal size (Scheme 1); Whereas an α of 0.88 observed from the PSCs based on the $(4F\text{-}PEA)_2PbI_4$:$MAPbI_3$ thin film demonstrates that the bimolecular recombination is significantly suppressed. Thus, the PSCs based on the $(4F\text{-}PEA)_2PbI_4$:$MAPbI_3$ thin film exhibit enhanced J_{SC} [53,54]. On the other hand, the slope of the fitting line for the V_{OC} vs. I is described as nKT/q, where n is the ideality factor, k is the Boltzmann constant, T is the absolute temperature and q is the elementary charge, respectively. The value of the slope is associated with the degree of trap-assisted charge recombination within PSCs [54,55]. The PSCs based on the $(4F\text{-}PEA)_2PbI_4$:$MAPbI_3$ thin film have a slope of 0.040 (1.54 kT/q), which is smaller than that (0.048, 1.85 kT/q) from the PSCs based on the 3D $MAPbI_3$ thin films. Such small slop indicates that the trap-assisted charge recombination within the PSCs based on the $(4F\text{-}PEA)_2PbI_4$:$MAPbI_3$ thin film is effectively suppressed, which can be ascribed to the reduced trap density of the $(4F\text{-}PEA)_2PbI_4$:$MAPbI_3$ thin film. As a result, the PSCs based on the $(4F\text{-}PEA)_2PbI_4$:$MAPbI_3$ thin film exhibit boosted J_{SC}.

The shelf stability of unencapsulated PSCs measured in the ambient atmosphere in the air with a relative humidity of ~30% is shown in Fig. 4d. The PSCs based on the 3D $MAPbI_3$ thin film show an apparent degradation in PCEs and maintain 50% of their initial PCE after 430 h (hrs). In contrast, the PSCs based on the $(4F\text{-}PEA)_2PbI_4$:$MAPbI_3$ thin film maintain 50% of its initial PCE for nearly 5000 h. Moreover, for the PSCs based on the $(4F\text{-}PEA)_2PbI_4$:$MAPbI_3$ thin film, both V_{OC} and FF are kept unchanged for more than 3600 h, but J_{SC} is decreased along with the aging time; whereas, for the PSCs based on the 3D $MAPbI_3$ thin film, V_{OC}, J_{SC}, and FF are decreased along with the aging time (Fig. S6).

The device performances of the PPDs with the same device structure as the PSCs described above are also studied. The J-V characteristics of PPDs measured at room temperature (RT) and under a monochromatic light at λ of 500 nm with the light intensity of 0.28 mW/cm^2 and in dark are shown in Fig. 5a. Compared to the PPDs based on the 3D $MAPbI_3$ thin film, the PPDs based on the $(4F\text{-}PEA)_2PbI_4$:$MAPbI_3$ thin film possess

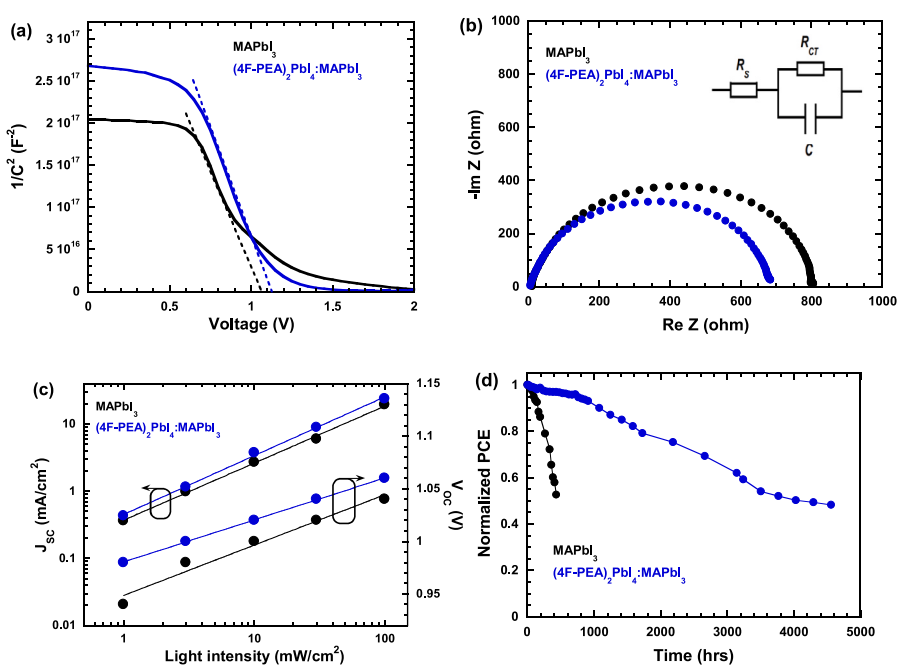

Fig. 4. (a) The C–V characteristics, (b) impedance spectra, (c) J_{SC}, V_{OC} versus the light intensity measurements of the PSCs, and (d) the stability of un-encapsulated PSCs, where the PSCs are based on either $MAPbI_3$ thin film or $(4F\text{-}PEA)_2PbI_4$:$MAPbI_3$ thin film.

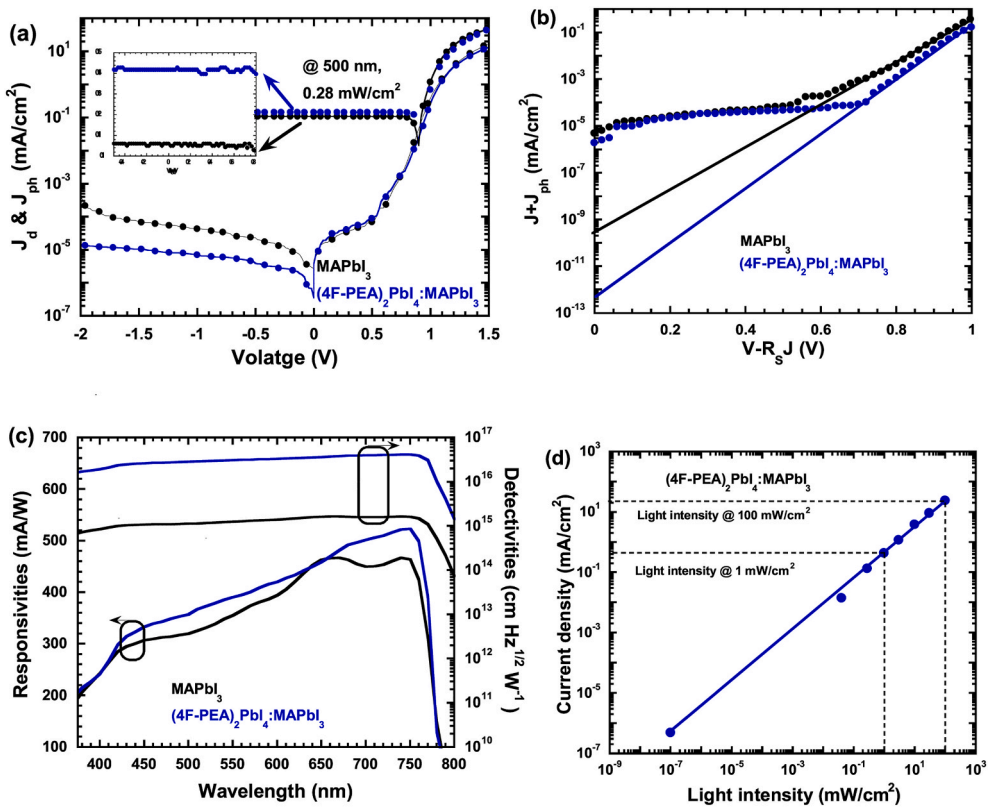

Fig. 5. (a) The J-V characteristics of the PPDs measured under monochromatic light at a wavelength (λ) of 500 nm with the light intensity of 0.28 mW/cm^2 and in dark (b) the plot of ln(J + J_{ph}) versus (V-R_ST) and the linear fitting of the PPDs, (c) the responsivities and detectivities of the PPDs, and (d) the linear dynamic range of the PPDs, where the PPDs are fabricated by either $MAPbI_3$ thin film or e $(4F\text{-}PEA)_2PbI_4$:$MAPbI_3$ thin film.

larger photocurrent density (J_{ph}) and smaller dark current density (J_{dark}), indicating that the PPDs based on the $(4F\text{-}PEA)_2PbI_4$:$MAPbI_3$ thin film exhibit superior responsibility (R) and projected detectivity (D*) as well [53]. On the other hand, based on the $V_{OC} = \left(nKT * \ln J_{ph}/J_0\right)/q$, where J_0 is reverse saturated J_{dark}, q is the electron charge, k is Boltzmann's constant, and T is the temperature [54], respectively, a small J_o observed from the PPDs based on the $(4F\text{-}PEA)_2PbI_4$:$MAPbI_3$ thin film indicates that the PSCs based on the $(4F\text{-}PEA)_2PbI_4$:$MAPbI_3$ thin film possess a larger V_{OC} compared to the PSCs based on the 3D $MAPbI_3$ thin film, which is consistent with the J-V characteristics (Fig. 3a).

For two-terminal diodes, J is described as $J = J_0\left[\exp\left(\frac{q(V-JR_s)}{nk_bT}\right) - 1\right] - J_{ph}$, where J is the total current density, V is the applied voltage, q is the elementary electron charge, R_S is the series resistance, n is the ideal factor, k_b is the Boltzmann constant, T is the absolute temperature, and J_{ph} is the photocurrent [56–58]. Thus, the ln(J_{ph} + J) versus the (V – R_SJ) and their linear fittings are shown in Fig. 5b. The J_0 for the PPDs based on the 3D $MAPbI_3$ thin film is 2.53 × 10^{-10} mA/cm^2, which is larger than that (4.99 × 10^{-13} mA/cm^2) observed from the PPDs based on the $(4F\text{-}PEA)_2PbI_4$:$MAPbI_3$ thin film, indicating that the PPDs based on the $(4F\text{-}PEA)_2PbI_4$:$MAPbI_3$ thin film exhibit suppressed J_d, consequently, boosted D*. According to the equation of $R = \frac{EQE*q}{h\nu} = (EQE * \lambda)/1240$ (where q is the elementary charge, h is the Planck constant, ν is the frequency of the incident light and λ is the wavelength) and based on the EQE spectra (Fig. 3b) [58], the R is calculated. The R values of PPDs are shown in Fig. 5c. The R values of the PPDs based on the 3D $MAPbI_3$ thin film are smaller than those based on the $(4F\text{-}PEA)_2PbI_4$:$MAPbI_3$ thin film. For example, at λ of 500 nm, the R of the PPDs based on the 3D $MAPbI_3$ thin film is 0.378 A/W, whereas the R of the PPDs based on the $(4F\text{-}PEA)_2PbI_4$:$MAPbI_3$ thin film is 0.504 A/W.

The D^* is described as $D^* = R/\sqrt[2]{2qJ_d}$ [59]. Based on the J_d (Fig. 5b) and R, the D^* versus wavelength (λ) is obtained, and the results are shown in Fig. 5c. It is found that the D^* values from the PPDs based on the 3D $MAPbI_3$ thin film are smaller than those based on the $(4F\text{-}PEA)_2PbI_4$:$MAPbI_3$ thin film. For example, at λ of 500 nm, the D^* of the PPDs based on the 3D $MAPbI_3$ thin film is 1.33 × 10^{15} Jones, whereas the D^* of the PPDs based on the $(4F\text{-}PEA)_2PbI_4$:$MAPbI_3$ thin film is 3.99 × 10^{16} Jones. Thus, the PPDs based on $(4F\text{-}PEA)_2PbI_4$:$MAPbI_3$ thin film exhibit boosted D^*.

Fig. 5d presents the linear dynamic range (LDR) of PPDs. The LDR (or photosensitivity linearity) (typically quoted in dB), is another key parameter used to evaluate photodetectors (PDs), which is described as $LDR = 20\log(J^*_{ph}/J_d)$, where J^*_{ph} is the J_{ph} measured at the light intensity of 1 mW cm^{-2} [59]. At RT, the LDR of the PPDs based on the $(4F\text{-}PEA)_2PbI_4$:$MAPbI_3$ thin film is 110 dB, which is higher than that (95 dB) of the PPDs based on the 3D $MAPbI_3$ thin film. Such a large LDR is comparable to that of Si-based PDs (120 dB, at 77 K) and is significantly higher than that (66 dB, at 4.2 K) of InGaAs-based PDs [57].

In addition, the results shown in Fig. 3d indicate that the PPDs based on the $(4F\text{-}PEA)_2PbI_4$:$MAPbI_3$ thin film exhibit a fast response time compared to that based on the 3D $MAPbI_3$ thin film.

4. Conclusion

In conclusion, we reported novel 2D perovskites, which were based on 4F-PEA organic spacer, which possesses a larger dipole moment compared to PEA, a widely used organic spacer, and further form the 2D mixed 3D perovskite composites. Systematically studies indicated that the 2D:3D mixed perovskite thin film possessed superior film morphology, larger crystal, and higher crystallinity compared to 3D

perovskite thin film. Moreover, we investigated the device performance of perovskite photovoltaics based on the 2D:3D mixed perovskite composite thin film, which exhibited over 21.16 ± 0.53% power conversion efficiency with suppressed photocurrent hysteresis, over 10^{16} cm $Hz^{1/2}W^{-1}$ detectivity, and dramatically boosted stability. Our results indicated that we provided a facile way to approach high-performance perovskite photovoltaics.

Declaration of competing interest

The authors declare that they have no known competing financial interests or personal relationships that could have appeared to influence the work reported in this paper.

Data availability

Data will be made available on request.

Acknowledgments

The authors acknowledge the National Science Foundation (NSF) (ECCS/EPMD1903303) and Air Force Office of Scientific Research (AFOSR) (through the Organic Materials Chemistry Program, Grant Number: FA9550-22-1-0488, Program Manager, Dr. Kenneth Caster) for financial supports.

Appendix A. Supplementary data

Supplementary data to this article can be found online at https://doi.org/10.1016/j.orgel.2023.106796.

References

[1] J. Seo, J.H. Noh, S.I. Seok, Rational strategies for efficient perovskite solar cells, Accounts, Chem. Res. 49 (2016) 562–572.
[2] M. Grätzel, The rise of highly efficient and stable perovskite solar cells, Accounts Chem. Res. 50 (2017) 487–491.
[3] A. Kojima, K. Teshima, Y. Shirai, T. Miyasaka, Organometal halide perovskites as visible-light sensitizers for photovoltaic cells, J. Am. Chem. Soc. 131 (2009) 6050–6051.
[4] https://www.nrel.gov/pv/assets/pdfs/best-research-cell-efficiencies-rev220126b.pdf.
[5] T.A. Berhe, W.-N. Su, C.-H. Chen, C.-J. Pan, J.-H. Cheng, H.-M. Chen, M.-C. Tsai, L.-Y. Chen, A.A. Dubale, B.-J. Hwang, Organometal halide perovskite solar cells: degradation and stability, Energy Environ. Sci. 9 (2016) 323–356.
[6] N.G. Park, M. Gratzel, T. Miyasaka, K. Zhu, K. Emery, Towards stable and commercially available perovskite solar cells, Nat. Energy 1 (2016) 1–8.
[7] Z.N. Song, A. Abate, S.C. Watthage, G.K. Liyanage, A.B. Phillips, U. Steiner, M. Graetzel, M.J. Heben, Perovskite solar cell stability in humid air: partially reversible phase transitions in the PbI_2-CH_3NH_3I-H_2O system, Adv. Energy Mater. 6 (2016), 1600846.
[8] F. Li, H. Wang, D. Kufer, L.L. Liang, W.L. Yu, E. Alarousu, C. Ma, Y.Y. Li, Z.X. Liu, C. X. Liu, N.N. Wei, F. Wang, L. Chen, O.F. Mohammed, A. Fratalocchi, X.G. Liu, G. Konstantatos, T. Wu, Ultrahigh carrier mobility achieved in photoresponsive hybrid perovskite films via coupling with single-walled carbon nanotubes, Adv. Mater. 29 (2017), 1602432.
[9] S.W. Wang, H.Y. Li, B.W. Zhang, Z.A. Guo, H. Bala, S.J. Yao, J.Y. Zhang, C. Chen, W.Y. Fu, J.L. Cao, G. Sun, Z.Y. Zhang, Perovskite solar cells based on the synergy between carbon electrodes and polyethylene glycol additive with excellent stability, Org. Electron. 83 (2020), 105734.
[10] H. Chen, W. Fu, C. Huang, Z. Zhang, S. Li, F. Ding, M. Shi, C.Z. Li, A.K.Y. Jen, H. Chen, Molecular engineered hole-extraction materials to enable dopant-free, efficient p-i-n perovskite solar cells, Adv. Energy Mater. 7 (2017), 1700012.
[11] K.O. Brinkmann, J. Zhao, N. Pourdavoud, T. Becker, T. Hu, S. Olthof, K. Meerholz, L. Hoffmann, T. Gahlmann, R. Heiderhoff, M.F. Oszajca, N.A. Luechinger, D. Rogalla, Y. Chen, B. Cheng, T. Riedl, Suppressed decomposition of organometal halide perovskites by impermeable electron-extraction layers in inverted solar cells, Nat. Commun. 8 (2017) 1–9.
[12] D. Koushik, W.J.H. Verhees, Y.H. Kuang, S. Veenstra, D. Zhang, M.A. Verheijen, M. Creatore, R.E.I. Schropp, High-efficiency humidity-stable planar perovskite solar cells based on atomic layer architecture, Energy Environ. Sci. 10 (2017) 91–100.
[13] W.M. Qiu, A. Ray, M. Jaysankar, T. Merckx, J.P. Bastos, D. Cheyns, R. Gehlhaar, J. Poortmans, P. Heremans, An interdiffusion method for highly performing cesium/formamidinium double cation perovskites, Adv. Funct. Mater. 27 (2017), 1700920.
[14] S.D. Yang, W.Q. Liu, L.J. Zuo, X.Q. Zhang, T. Ye, J.H. Chen, C.Z. Li, G. Wu, H. Z. Chen, Thiocyanate assisted performance enhancement of formamidinium based planar perovskite solar cells through a single one-step solution process, J. Mater. Chem. 4 (2016) 9430–9436.
[15] Q. Dong, F.Z. Liu, M.K. Wong, H.W. Tam, A.B. Djurisic, A.N. Ng, C. Surya, W. K. Chan, A.M.C. Ng, Encapsulation of perovskite solar cells for high humidity conditions, ChemSusChem 9 (2016) 2597–2603.
[16] K. Domanski, J.P. Correa-Baena, N. Mine, M.K. Nazeeruddin, A. Abate, M. Saliba, W. Tress, A. Hagfeldt, M. Gratzel, Not all that glitters is gold: metal-migration-induced degradation in perovskite solar cells, ACS Nano 10 (2016) 6306–6314.
[17] S.N. Habisreutinger, T. Leijtens, G.E. Eperon, S.D. Stranks, R.J. Nicholas, H. J. Snaith, Carbon nanotube/polymer composites as a highly stable hole collection layer in perovskite solar cells, Nano Lett. 14 (2014) 5561–5568.
[18] T. Zhu, Y. Yang, K. Gu, C. Liu, J. Zheng, X. Gong, Novel quasi-2D perovskites for stable and efficient perovskite solar cells, ACS Appl. Mater. Interfaces 12 (2020), 51844-51755.
[19] I.C. Smith, E.T. Hoke, D. Solis-Ibarra, M.D. McGehee, H.I. Karunadasa, A layered hybrid perovskite solar-cell absorber with enhanced moisture stability, Angew. Chem. 126 (2014) 11414–11417.
[20] T. Luo, Y.L. Zhang, Z. Xu, T.Q. Niu, J.L. Wen, J. Lu, S.Y. Jin, S.Z. Liu, K. Zhao, Compositional control in 2d perovskites with alternating cations in the interlayer space for photovoltaics with efficiency over 18, Adv. Mater. 31 (2019), 1903848.
[21] J. Shi, Y. Gao, X. Gao, Y. Zhang, J. Zhang, X. Jing, M. Shao, Fluorinated low-dimensional Ruddlesden-Popper perovskite solar cells with over 17% power conversion efficiency and improved stability, Adv. Mater. 31 (2019), 1901673.
[22] H. Tsai, W. Nie, J.-C. Blancon, C.C. Stoumpos, R. Asadpour, B. Harutyunyan, A. J. Neukirch, R. Verduzco, J.J. Crochet, S. Tretiak, High-efficiency two-dimensional Ruddlesden–Popper perovskite solar cells, Nature 536 (2016) 312–316.
[23] Y. Qin, H. Zhong, J.J. Intemann, S. Leng, M. Cui, C. Qin, M. Xiong, F. Liu, A.K. Y. Jen, K. Yao, Coordination engineering of single-crystal precursor for phase control in Ruddlesden–Popper perovskite solar cells, Adv. Energy Mater. 10 (2020), 1904050.
[24] Z. Chen, B. Turedi, A.Y. Alsalloum, C. Yang, X. Zheng, I. Gereige, A. AlSaggaf, O. F. Mohammed, O.M. Bakr, Single-crystal $MAPbI_3$ perovskite solar cells exceeding 21% power conversion efficiency, ACS Energy Lett. 4 (2019) 1258–1259.
[25] C. Fei, M. Zhou, J. Ogle, D.-M. Smilgies, L. Whittaker-Brooks, H. Wang, Self-assembled propylammonium cations at grain boundaries and the film surface to improve the efficiency and stability of perovskite solar cells, J. Mater. Chem. 7 (2019) 23739–23746.
[26] L. Zheng, L. Shen, T. Zhu, D. Zhang, J. Zheng, X. Gong, Stable and efficient perovskite solar cells by discrete two-dimensional perovskites capped on the three-dimensional perovskites bilayer thin film, Nano Energy 96 (2022), 107126.
[27] R. Chen, L. Shen, L. Zheng, T. Zhu, Y. Liu, L. Liu, J. Zheng, X. Gong, Two-/three-dimensional perovskite bilayer thin films post-treated with solvent vapor for high-performance perovskite photovoltaics, ACS Appl. Mater. Interfaces 13 (2021) 49104–49113.
[28] H.L. Loi, J. Cao, X. Guo, C.K. Liu, N. Wang, J. Song, G. Tang, Y. Zhu, F. Yan, Gradient 2D/3D perovskite films prepared by hot-casting for sensitive photodetectors, Adv. Sci. 7 (2020), 2000776.
[29] X. Zhang, C. Ji, X. Liu, S. Wang, L. Li, Y. Peng, Y. Yao, M. Hong, J. Luo, Solution-grown large-sized single-crystalline 2D/3D perovskite heterostructure for self-powered photodetection, Adv. Opt. Mater. 8 (2020), 2000311.
[30] M.L. Tang, Z. Bao, Halogenated materials as organic semiconductors, Chem. Mater. 23 (2011) 446–455.
[31] J.S. Shi, Y.R. Gao, X. Gao, Y. Zhang, J.J. Zhang, X. Jing, M. Shao, Fluorinated low-dimensional Ruddlesden–Popper perovskite solar cells with over 17% power conversion efficiency and improved stability, Adv. Mater. 31 (2019), 1901673.
[32] K. Wang, L. Zheng, T. Zhu, X. Yao, C. Yi, X. Zhang, Y. Cao, L. Liu, W. Hu, X. Gong, Efficient perovskite solar cells by hybrid perovskites incorporated with heterovalent neodymium cations, Nano Energy 61 (2019) 352–360.
[33] Z. Jiang, X. Li, J. Strzalka, M. Sprung, T. Sun, A.R. Sandy, S. Narayanan, D.R. Lee, J. Wang, The dedicated high-resolution grazing-incidence X-ray scattering beamline 8-ID-E at the Advanced Photon Source, J. Synchrotron, Radiata 19 (2012) 627–636.
[34] C. Fei, J.S. Sarmiento, H. Wang, Generation of coherent optical phonons in methylammonium lead iodide thin films, J. Phys. Chem. C 122 (2018) 17035–17041.
[35] X. Zhao, T. Liu, Y.-L. Loo, Advancing 2D perovskites for efficient and stable solar cells: challenges and opportunities, Adv. Mater. 34 (2022), 2105849.
[36] F. Li, S. Zhou, J. Yuan, C. Qin, Y. Yang, J. Shi, X. Ling, Y. Li, W. Ma, Perovskite quantum dot solar cells with 15.6% efficiency and improved stability enabled by an α-$CsPbI_3$/$FAPbI_3$ bilayer structure, ACS Energy Lett. 4 (2019) 2571–2578.
[37] J. Zhang, X. Liu, P. Jiang, H. Chen, Y. Wang, J. Ma, R. Zhang, F. Yang, M. Wang, J. Zhang, Red-emitting $CsPbBrI_2$/PbSe heterojunction nanocrystals with high luminescent efficiency and stability for bright light-emitting diodes, Nano Energy 66 (2019), 104142.
[38] H. Tsai, R. Asadpour, J.-C. Blancon, C.C. Stoumpos, O. Durand, J.W. Strzalka, B. Chen, R. Verduzco, P.M. Ajayan, S. Tretiak, Light-induced lattice expansion leads to high-efficiency perovskite solar cells, Science 360 (2018) 67–70.
[39] L. Zheng, K. Wang, T. Zhu, Y. Yang, R. Chen, K. Gu, C. Liu, X. Gong, High-performance perovskite solar cells by one-step self-assembled perovskite-polymer thin films, ACS Appl. Energy Mater. 3 (2020) 5902–5912.
[40] H.-S. Kim, N.-G. Park, Parameters affecting I–V hysteresis of $CH_3NH_3PbI_3$ perovskite solar cells: effects of perovskite crystal size and mesoporous TiO_2 layer, J. Phys. Chem. Lett. 5 (2014) 2927–2934.

[41] D. Glowienka, D. Zhang, F. Di Giacomo, M. Najafi, S. Veenstra, J. Szmytkowski, Y. Galagan, Role of surface recombination in perovskite solar cells at the interface of HTL/$CH_3NH_3PbI_3$, Nano Energy 67 (2020), 104186.
[42] S. van Reenen, M. Kemerink, H.J. Snaith, Modeling anomalous hysteresis in perovskite solar cells, J. Phys. Chem. Lett. 6 (2015) 3808–3814.
[43] J. Seifter, Y. Sun, A.J. Heeger, Transient photocurrent response of small-molecule bulk heterojunction solar cells, Adv. Mater. 26 (2014) 2486–2493.
[44] K. Wang, L. Zheng, T. Zhu, L. Liu, M.L. Becker, X. Gong, High performance perovskites solar cells by hybrid perovskites co-crystallized with poly(ethylene oxide), Nano Energy 67 (2020), 104229.
[45] T. Zhu, Y. Yang, K. Gu, C. Liu, J. Zheng, X. Gong, Novel quasi-2D perovskites for stable and efficient perovskite solar cells, ACS Appl. Mater. Interfaces 12 (2020) 51744–51755.
[46] B. Cheng, T.-Y. Li, P.-C. Wei, J. Yin, K.-T. Ho, J.R.D. Retamal, O.F. Mohammed, J.-H. He, Layer-edge device of two-dimensional hybrid perovskites, Nat. Commun. 9 (2018) 1–7.
[47] P. Murgatroyd, Theory of space-charge-limited current enhanced by Frenkel effect, J. Phys. D Appl. Phys. 3 (1970) 151.
[48] J.M. Luther, M. Law, M.C. Beard, Q. Song, M.O. Reese, R.J. Ellingson, A.J. Nozik, Schottky solar cells based on colloidal nanocrystal films, Nano Lett. 8 (2008) 3488–3492.
[49] R.H. Bube, Trap density determination by space-charge-limited currents, J. Appl. Phys. 33 (1962) 1733–1737.
[50] O.J. Sandberg, J. Kurpiers, M. Stolterfoht, D. Neher, P. Meredith, S. Shoaee, A. Armin, On the question of the need for a built-in potential in perovskite solar cells, Adv. Mater. Interfac. 7 (2020), 2000041.
[51] V. Gonzalez-Pedro, E.J. Juarez-Perez, W.-S. Arsyad, E.M. Barea, F. Fabregat-Santiago, I. Mora-Sero, J. Bisquert, General working principles of $CH_3NH_3PbX_3$ perovskite solar cells, Nano Lett. 14 (2014) 888–893.
[52] H. Lai, B. Kan, T. Liu, N. Zheng, Z. Xie, T. Zhou, X. Wan, X. Zhang, Y. Liu, Y. Chen, Two-dimensional Ruddlesden–Popper perovskite with nanorod-like morphology for solar cells with efficiency exceeding 15, J. Am. Chem. Soc. 140 (2018) 11639–11646.
[53] T. Singh, T. Miyasaka, Stabilizing the efficiency beyond 20% with a mixed cation perovskite solar cell fabricated in ambient air under controlled humidity, Adv. Energy Mater. 8 (2018), 1700677.
[54] S.M. Sze, Y. Li, K.K. Ng, Physics of Semiconductor Devices, John Wiley & Sons, 2021.
[55] T. Zhu, L. Shen, D. Zhang, J. Zheng, X. Gong, Solution-processed ternary perovskite-organic broadband photodetectors with ultrahigh detectivity, ACS Appl. Mater. Interfaces 14 (2022) 18744–18750.
[56] G. Wetzelaer, M. Kuik, M. Lenes, P. Blom, Origin of the dark-current ideality factor in polymer: fullerene bulk heterojunction solar cells, Appl. Phys. Lett. 99 (2011), 153506.
[57] A.R. Jha, A.R. Jha, D.A. Jha, Infrared Technology: Applications to Electrooptics, Photonic Devices, and Sensors, Wiley, New York, 2000.
[58] H. Dong, H. Zhu, Q. Meng, X. Gong, W. Hu, Organic photoresponse materials and devices, Chem. Soc. Rev. 41 (2012) 1754–1808.
[59] X. Gong, M. Tong, Y. Xia, W. Cai, J.S. Moon, Y. Cao, G. Yu, C.-L. Shieh, B. Nilsson, A.J. Heeger, High-detectivity polymer photodetectors with spectral response from 300 nm to 1450 nm, Science 325 (2009) 1665–1667.